APPLAuSE

Review Letters | 2023

VOXEL

Cover: Commemoration of the 30 years of GoLP. This image was taken with a CCD camera at the focus of an 800 nm laser reflecting from a Spatial Light Modulator. This device allows to control the wavefronts of the laser permitting the reconstruction of images at the Fourier plane, Gonçalo Vaz.

Universidade de Lisboa

Instituto Superior Técnico

APPLAuSE Review Letters

Authors:
Diogo Silva
Gonçalo Vaz
Lucas Ansia
Óscar Amaro

Editor:
Marta Fajardo

November 2022

Contents

Editor foreword

Welcome to the latest issue of APPLAUSE Review Letters, where we showcase the insightful work of our talented PhD students. This edition highlights the diverse research topics explored by APPLAuSE, including the valuable contributions of a student invited from the Center of Astrophysics and Gravitation (CENTRA).

I would like to express my gratitude to our students for their exceptional dedication. Although our cohort comprises only four students, this edition highlights their significant contributions and collaborative spirit, making this journey truly rewarding. I also extend my appreciation to our guest editor, Lucas Ansia for his effort in shaping this edition.

Furthermore, I would like to thank the reviewers for their invaluable feedback, which has contributed to the quality of this publication. We invite you to explore this edition of APPLAUSE Review Letters.

Marta Fajardo,
Editor, APPLAuSE Review Letters,
Instituto de Plasmas e Fusão Nuclear (IPFN), Instituto Superior Técnico.

Guest Editor foreword

Within the pages of this edition, we present a compilation of the work done by the APPLAuSE PhD program fellows, together with our invited student from CENTRA.

While our focus in academia often centres on research outcomes, especially at the beginning of our career, it is important to recognize that science encompasses more than results. This magazine and our soft skill course serve as a reminder that effectively share our research is an integral part of the scientific process.

I want to thank all the students that take part in the course as well as our professor, Marta Fajardo, for all their interest and their uncountable contributions. I would also like to thank the APPLAuSE PhD program, not only for this workshop but for the opportunities to pursue my doctoral studies under their support.

I really hope you enjoy reading this magazine as much as we enjoy building it.

Lucas Ansia,
APPLAuSE PhD student,
Instituto de Plasmas e Fusão Nuclear (IPFN), Instituto Superior Técnico.

Best Image Award

This year's best figure winner is Diogo Silva.

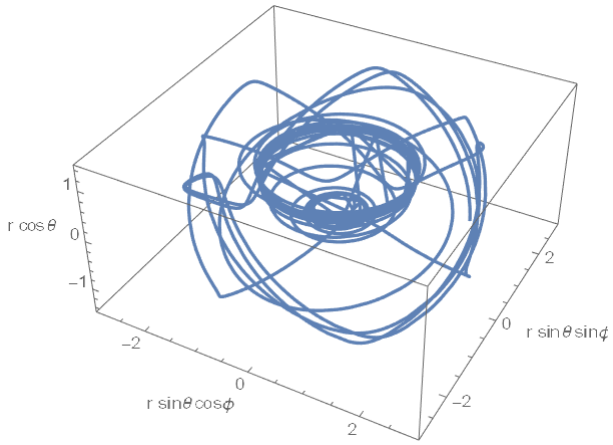

Trajectory of a falling timelike particle, in (r, θ, ϕ) coordinates, and beginning fall from the ISSO with $(a, r_I) = (0.9, 2.6)$. After initiating fall, the particle reaches the outer and interior event horizons, r_+ and r_-, respectively, before reaching the ring singularity at the center.

About us

Diogo Silva was born in Lisbon. He finished his Master's Degree in Engineering Physics in 2020 having developed his thesis on the subject of gravitation with focus on gravitational collapse of dust, at CENTRA. In 2022 he started his PhD in the same research group, under the supervision of professors Jorge Rocha and David Hilditch, and was awarded an FCT grant. His PhD thesis, also on gravitational collapse in general relativity, focuses on more complex matter models with the objective to better improve the current understanding of these phenomena.

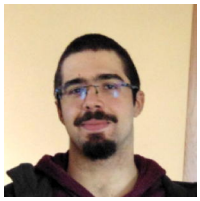

Gonçalo Vaz was born in 1998, in Guarda, Portugal. In 2016 initiated an Integrated Master's in Engineering Physics at IST, later joining the Group of Lasers and Plasmas in 2020 as an intern. The following year, he concluded his MSc in this group under the supervision of Drs. Gonçalo Figueira and Hugo Pires, with a thesis titled: Nonlinear optics with ultrashort mid-infrared laser pulses. Presently he is enrolled in the APPLAuSE program exploring the capabilities of high-power laser sources and nonlinear optics in the laboratory.

Lucas Ansia was born in the small town of Ourense, Galicia. As a Master's student, he worked at the Fusion Institute of the Polytechnic University of Madrid, where he obtained his Master's degree in Nuclear Science and Technology in 2021. His thesis focused on the development of multi-material hydrodynamic codes. In 2022 he joined the APPLAuSE program and started his PhD under the supervision of Prof. Marta Fajardo and Dr. Gareth Williams, on the modelling of laser driven solid-density plasmas.

Óscar Amaro obtained his MSc Degree in Engineering Physics in 2021, from IST. He is currently developing his PhD under the supervision of Prof. Marija Vranic on QED-Plasma Physics and Quantum Algorithms within the APPLAuSE program. This work addresses issues such as optimal positron production in laser-electron scattering in current and near-future Petawatt facilities and the possibility of using quantum computers to solve plasma physics problems. Before enrolling in the APPLAuSE program, he joined GoLP-EPP as an undergraduate student in 2018.

Analytic Solutions of Geodesics in Rotating Spacetime*

Diogo Silva[1]

***Abstract*— Starting from the Kerr metric in Kerr-Newman coordinates we develop the analytic solutions for test particles that fall from the innermost precessing stable circular orbit (ISSO). We show that application of the Mino time parameterization to the equations of motion found by Carter allows a closed form solution through the use of elliptic functions. The solution hence obtained depends only on the constants of the motion, corresponding to the Carter constant, energy and angular momentum, but also on the roots of the radial and polar potentials. Having obtained the description of this system, we obtain a better understanding of particle dynamics in curved spacetimes, thus serving as an important stepping stone for other dyamical systems such as compact object binaries.**

I. INTRODUCTION

The complete description of geodesics induced by a black hole is an important part of understanding the causal structure of spacetime [1]. While the geodesic equations for the Schwarzschild black hole, the oldest and most studied vacuum solution, are well known [2], the same is not true for the geodesics surrounding the Kerr black hole. Discovered by Kerr [3], it has been studied extensively, with regard to its properties, by Carter [4] and written in different coordinate systems, e.g., by Newman *et al.* [5]. In his works, Carter [4] obtained the equations of motion for falling test particles. However, the complexity shown by this spacetime has made analytic solutions for the corresponding geodesics elusive. Mino [6], while employing a perturbative method to obtain the orbits of particles, proposed a parameterization that simplifies the equations of motion, but did not obtain an explicit closed form solution. This solution was found recently by Dyson and van de Meent [7] who, following on Mino's work, showed that solutions for generalized falling test particles could be obtained in the form of elliptic functions. A closed form description of geodesics of falling particles is a matter of great importance, as it not only gives the causal structure of the spacetime around the black hole, i.e. how observers report events around them, but can also be used to describe phenomena involving rotating black holes.

In this report we start from the work of Carter and develop the system of equations onward in a unified notation for the specific case of the innermost precessing stable circular orbits (ISSO). This is not limiting as the only restriction comes in the form of the roots of a radial potential. Obtaining the generalized solution requires only dropping that restriction, but otherwise the mathematical methods are equivalent.

*This work was supported by FCT though the grant 2022.13617.BD

[1]D. Silva is with CENTRA- center for astrophysics and gravitation, Instituto Superior Técnico- Universidade de Lisboa, Avenida Rovisco Pais 1, 1049-001 Lisbon, Portugal Diogo L. F. G. Silva at orcid.org Corresponding author: diogo.l.silva@tecnico.ulisboa.pt

Corresponding author: diogo.l.silva@tecnico.ulisboa.pt

The report's layout is as follows. In Section II we obtain the differential equations of geodesic motion for the rotating metric, as obtained by Carter, carefully explaining each step. In Section III we apply the restriction to the ISSO by restricting the radial potential and its number of roots. In Section IV we present the conclusions of this work and possible venues for future research.

In this report we use natural units, i.e. $G = c = 1$, and a negative metric signature, i.e. $\mathrm{diag}(-1,1,1,1)$.

II. EQUATIONS OF GEODESIC MOTION

A. For a General Metric

A metric defines the distance relation between adjacent points in spacetime. As particles follow paths that maximize the distance, called geodesics, we start by defining a metric specifying the spacetime. We define the general case

$$\mathrm{d}s^2 = g_{ij}\,\mathrm{d}x^i\,\mathrm{d}x^j, \tag{1}$$

The metric establishes the canonical momenta

$$p_i = g_{ij}\dot{x}^j, \tag{2}$$

where an overdot denotes differentiation with respect to the parameter of the path, i.e., $\dot{x} = \mathrm{d}x/\mathrm{d}\tau$, τ being the proper time. The particles' Lagrangian can then be defined as

$$L = \frac{1}{2}\,g_{ij}\dot{x}^i\dot{x}^j = -\frac{1}{2}\,\mu^2, \tag{3}$$

with μ^2 a constant of values $\mu = 0,-1,1$ for null, spacelike and timelike geodesics, respectively. Note that μ^2 is normalization factor and its value can, apart from the sign, be changed through reparameterization. The Hamiltonian is defined as

$$H = \frac{1}{2}\,g^{ij}\,p_i\,p_j = -\frac{1}{2}\,\mu^2 \tag{4}$$

The equations of motion can be obtained through the Hamilton-Jacobi equation.

$$S = \frac{1}{2}\,\mu^2\,\tau + S_u + S_r + S_z + S_{\bar{\phi}} \tag{5}$$

where S is the Hamilton Principal Function (HPF) and is defined through

$$\frac{\partial S}{\partial \tau} = -H \quad , \quad \frac{\partial S}{\partial q^i} = \frac{\partial L}{\partial \dot{q}^i} = p_i, \tag{6}$$

for coordinates q^i. On the other hand, derivatives of the HPF with respect to the constants of motion, α_j, are constant

$$\frac{\partial S}{\partial \alpha_j} = 0, \tag{7}$$

thus yielding the equations of motion.

B. For the Kerr Metric

For a rotating black hole, we consider the Kerr metric in Kerr-Newman coordinates,

$$\begin{aligned} \mathrm{d}s^2 = &-\left(1-\frac{2Mr}{\Sigma}\right)\mathrm{d}u^2 + 2\,\mathrm{d}u\,\mathrm{d}r - 2\frac{2Mr}{\Sigma}a\,(1-z^2)\,\mathrm{d}u\,\mathrm{d}\bar{\phi} \\ &- 2a\,(1-z^2)\,\mathrm{d}r\,\mathrm{d}\bar{\phi} + \frac{\Sigma}{1-z^2}\,\mathrm{d}z^2 \\ &+ \frac{1}{\Sigma}\left((r^2+a^2)^2 - \Delta a^2\,(1-z^2)\right)(1-z^2)\,\mathrm{d}\bar{\phi}^2, \end{aligned} \tag{8}$$

where

$$\Sigma = r^2 + a^2 z^2 \quad , \quad \Delta = r^2 - 2Mr + a^2, \tag{9}$$

and a and M are the spin and mass of the black hole, respectively. The coordinates $(u, z, \bar{\phi})$ are related to the usual coordinates (t, θ, ϕ) through

$$\mathrm{d}u = \mathrm{d}t + \frac{2Mr+\Delta}{\Delta}\mathrm{d}r \ , \ z = \cos\theta \ , \ \mathrm{d}\bar{\phi} = \mathrm{d}\phi + \frac{a}{\Delta}\mathrm{d}r. \tag{10}$$

The Kerr spacetime verifies two horizons, corresponding to the roots of Δ, respectively $r_\pm = M \pm \sqrt{M^2 - a^2}$, which exist only for $M > a$, which we will be considering onward. The momenta follow from Eq. (2)

$$p_u = -\left(1-\frac{2Mr}{\Sigma}\right)\dot{u} + \dot{r} - \frac{2Mr}{\Sigma}a\,(1-z^2)\,\dot{\bar{\phi}}, \tag{11}$$

$$p_r = \dot{u} - a\,(1-z^2)\,\dot{\bar{\phi}}, \tag{12}$$

$$p_z = \frac{\Sigma}{1-z^2}\,\dot{z}, \tag{13}$$

$$\begin{aligned} p_{\bar{\phi}} = &-\frac{2Mr}{\Sigma}a\,(1-z^2)\,\dot{u} - a\,(1-z^2)\,\dot{r} + \\ &+ \frac{1}{\Sigma}\left((r^2+a^2)^2 - \Delta a^2\,(1-z^2)\right)(1-z^2)\,\dot{\bar{\phi}}. \end{aligned} \tag{14}$$

The Lagrangian follows directly from the metric, Eq. (8), and the Hamiltonian follows from the momenta, Eqs. (11)-(14),

$$\begin{aligned} H = &\frac{1}{2}\left[\frac{1}{\Sigma}a^2\,(1-z^2)\,p_u^2 + 2\frac{1}{\Sigma}(r^2+a^2)\,p_u\,p_r + 2\frac{a}{\Sigma}p_u\,p_{\bar{\phi}} + \right. \\ &\left. + \frac{\Delta}{\Sigma}p_r^2 + 2\frac{a}{\Sigma}p_r\,p_{\bar{\phi}} + \frac{1-z^2}{\Sigma}p_z^2 + \frac{1}{\Sigma\,(1-z^2)}p_{\bar{\phi}}^2\right]. \end{aligned} \tag{15}$$

Returning to the HPF and from Eq. (6), each of its parts could be obtained as the integral of either the momenta or, equivalently, the quantity $\partial L/\partial \dot{q}^i$. The latter can be noted to be one of the terms of the Euler-Lagrange equation. Thus, noting also that the metric, and thus the Lagrangian, does not depend explicitly on either coordinates t and $\bar{\phi}$, we have two constants of motion in the form of the energy (ε) and angular momentum ($\mathscr{L}$) and

$$p_u = -\varepsilon \quad , \quad p_{\bar{\phi}} = \mathscr{L}, \tag{16}$$

$$\Longrightarrow S_u = -\varepsilon\,u \quad , \quad S_{\bar{\phi}} = \mathscr{L}\,\bar{\phi}. \tag{17}$$

Applying the remaining relations for S_r and S_z in the Hamiltonian, Eq. (15), we find terms that depend only on r and on z, i.e., the equation becomes separable. Introducing the constant $\mathscr{K}$, we then have

$$(1-z^2)\left(\frac{\partial S_z}{\partial z}\right)^2 + \mu^2 a^2 z^2 + (1-z^2)\left[a\,\varepsilon - \frac{\mathscr{L}}{1-z^2}\right]^2 = \mathscr{K}, \tag{18}$$

$$\Delta\left(\frac{\partial S_r}{\partial r}\right)^2 - 2\left[(r^2+a^2)\,\varepsilon - a\,\mathscr{L}\right]\left(\frac{\partial S_r}{\partial r}\right) + \mu^2 r^2 = -\mathscr{K}, \tag{19}$$

with the first directly solvable and the second solvable by quadrature, giving

$$\frac{\partial S_z}{\partial z} = \sqrt{\Theta}, \tag{20}$$

$$\frac{\partial S_r}{\partial r} = \Delta^{-1}\left(P + \sqrt{R}\right), \tag{21}$$

where

$$\Theta = Q - z^2\left[a^2(\mu^2 - \varepsilon^2) + \frac{\mathscr{L}}{1-z^2}\right], \tag{22}$$

$$P = (r^2+a^2)\,\varepsilon - a\,\varepsilon, \tag{23}$$

$$R = P^2 - \Delta\left[\mu^2 r^2 + Q + (\mathscr{L} - a\,\varepsilon)^2\right], \tag{24}$$

with $Q = \mathscr{K} - (\mathscr{L} - a\,\varepsilon)^2$ the Carter constant. We note again that Θ is a function of z only, $\Theta \equiv \Theta(z)$, while P and R are functions of r only, $P \equiv P(r)$ and $R \equiv R(r)$. The HPF is now

$$S = \frac{\mu^2}{2}\tau - \varepsilon\,u + \mathscr{L}\,\bar{\phi} + \int \Delta^{-1}\,(P + \sqrt{R})\,\mathrm{d}r + \int \sqrt{\frac{\Theta}{1-z^2}}\,\mathrm{d}z. \tag{25}$$

As mentioned before, the equations of motion can now be obtained by differentiation of the HPF, Eq. (25), with respect to the constants of motion, i.e., by using Eq. (7). Considering the set of constants as μ, ε, $\mathscr{L}$ and $\mathscr{K}$ (in place of Q), we obtain,

$$\begin{aligned} 0 &= \frac{\partial S}{\partial \mathscr{K}} \\ &\Longrightarrow \int \frac{1}{\sqrt{1-z^2}\sqrt{\Theta}}\,\mathrm{d}z = \int \frac{1}{\sqrt{R}}\,\mathrm{d}r, \end{aligned} \tag{26}$$

$$\begin{aligned} 0 &= \frac{\partial S}{\partial \mu} \\ &\Longrightarrow \tau = \int \frac{r^2}{\sqrt{R}}\,\mathrm{d}r + \int \frac{a^2 z^2}{\sqrt{1-z^2}\sqrt{\Theta}}\,\mathrm{d}z, \end{aligned} \tag{27}$$

$$\begin{aligned} 0 &= \frac{\partial S}{\partial \varepsilon} \\ &\Longrightarrow u = \int \frac{-a}{\sqrt{1-z^2}\sqrt{\Theta}}\left[a\,\varepsilon\,(1-z^2) - \mathscr{L}\right]\mathrm{d}z + \\ &\qquad + \int \frac{r^2+a^2}{\Delta}\left(1 + \frac{P}{\sqrt{R}}\right)\mathrm{d}r, \end{aligned} \tag{28}$$

$$\begin{aligned} 0 &= \frac{\partial S}{\partial \mathscr{L}} \\ &\Longrightarrow \bar{\phi} = -\int \frac{1}{\sqrt{1-z^2}\sqrt{\Theta}}\left[a\,\varepsilon - \frac{\mathscr{L}}{1-z^2}\right]\mathrm{d}z + \\ &\qquad + \int \frac{a}{\Delta}\left(1 + \frac{P}{\sqrt{R}}\right)\mathrm{d}r, \end{aligned} \tag{29}$$

and in these and henceforth we will fix $\mu = 1$ for test particles falling along timelike geodesics. While these already comprise the dynamics of test particles, their differential forms are more useful. Thus, by differentiating Eqs. (26)-(29), and working them out, we obtain

$$\Sigma \dot{r} = \sqrt{R}, \tag{30}$$

$$\Sigma \dot{z} = \sqrt{1-z^2}\sqrt{\Theta}, \tag{31}$$

$$\Sigma \dot{u} = -a\left[a\varepsilon(1-z^2) - \mathscr{L}\right] + (r^2+a^2)\Delta^{-1}(\sqrt{R}+P), \tag{32}$$

$$\Sigma \dot{\tilde{\phi}} = -\left(a\varepsilon - \frac{\mathscr{L}}{1-z^2}\right) + a\Delta^{-1}(\sqrt{R}+P). \tag{33}$$

With these forms, and following the dependencies of the Θ. P and R functions, we now use the proper time coordinate transformation due to Mino,

$$\mathrm{d}\tau = \Sigma \mathrm{d}\lambda, \tag{34}$$

with which the differential form of the equations of motion, Eqs. (30)-(33), and transforming the $\tilde{\phi}$ coordinate into ϕ, become

$$\left(\frac{\partial r}{\partial \lambda}\right)^2 = \left[(r^2+a^2)\varepsilon - a\mathscr{L}\right]^2 - \Delta\left[r^2 + Q + (\mathscr{L}-a\varepsilon)^2\right] = \\ = (1-\varepsilon^2)(r_1-r)(r_2-r)(r_3-3)(r_4-r) = \mathscr{R}(r), \tag{35}$$

$$\left(\frac{\partial z}{\partial \lambda}\right)^2 = Q - z^2\left[a^2(1-\varepsilon^2)(1-z^2) + \mathscr{L}^2 + Q\right] = \\ = (z^2-z_1^2)\left[a^2(1-\varepsilon^2)z^2 - z_2^2\right] = \mathscr{Z}(z), \tag{36}$$

$$\frac{\partial t}{\partial \lambda} = \frac{r^2+a^2}{\Delta}\left[(r^2+a^2)\varepsilon - a\mathscr{L}\right] - a^2\varepsilon(1-z^2) + a\mathscr{L}, \tag{37}$$

$$\frac{\partial \phi}{\partial \lambda} = \frac{a}{\Delta}\left[(r^2+a^2)\varepsilon - a\mathscr{L}\right] + \frac{\mathscr{L}}{1-z^2} - a\varepsilon. \tag{38}$$

And we now find that the first two equations, Eqs. (35) and (36), depend only on one variable each and can be solved directly. The other two, Eqs. (37) and (38) can be solved afterwards, completely specifying the dynamics of the test particle. We now evaluate the specific case where particles fall from the ISSO.

III. Solving the Equations for the ISSO

A. The Radial Equation

For this case, the radial potential, $\mathscr{R}(r)$, has a triple root at the radius corresponding to the ISSO, r_I. Then Eq. (35) becomes

$$\left(\frac{\partial r}{\partial \lambda}\right)^2 = (1-\varepsilon^2)(r_I - r)^3(r - r_4), \tag{39}$$

whereby comparison with Eq. (35) yields the other root r_4

$$r_4 = \frac{a^2 Q}{(1-\varepsilon^2) r_I^3}. \tag{40}$$

With this, we can now obtain the analytical solution directly. Solving Eq. (39), we obtain

$$r(\lambda) = \frac{r_I(r_I - r_4)^2(1-\varepsilon^2)\lambda^2 + 4 r_4}{(r_I - r_4)^2(1-\varepsilon^2)\lambda^2 + 4}. \tag{41}$$

B. The Polar Equation

Likewise, we can obtain the roots for the polar potential, Eq. (36), by comparing both sides of the equality. Doing so gives

$$z_1 = \sqrt{\frac{1}{2}\left(A - \sqrt{B}\right)} \quad , \quad z_2 = \sqrt{\frac{a^2(1-\varepsilon^2)}{2}\left(A + \sqrt{B}\right)}, \tag{42}$$

where

$$A = 1 + \frac{\mathscr{L}^2 + Q}{a^2(1-\varepsilon^2)} \quad , \quad B = A^2 - \frac{4Q}{a^2(1-\varepsilon^2)}. \tag{43}$$

and we define

$$k_z = a\sqrt{1-\varepsilon^2}\,\frac{z_1}{z_2}. \tag{44}$$

Then, for the differential equation, Eq. (36), we rewrite it as

$$\left(\frac{\partial z}{\partial \lambda}\right)^2 = (z^2 - z_1^2)\left[a^2(1-\varepsilon^2)z^2 - z_2^2\right] \\ \Longrightarrow \left(\frac{\partial \tilde{z}}{\partial \tilde{\lambda}}\right)^2 = (1-\tilde{z}^2)\left(1 - \frac{a^2(1-\varepsilon^2)z_1^2}{z_2^2}\tilde{z}^2\right),$$

where $\tilde{z} = z/z_1$ and $\tilde{\lambda} = z_2\lambda$. This can be recognized as the differential equation defining the Jacobi elliptic sine function [8][9]. Thus

$$z(\lambda) = z_1 \,\mathrm{sn}(z_2\lambda | k_z^2). \tag{45}$$

C. The Azimuthal Equation

For the azimuthal dependence, we start from the differential equation, Eq. (38), and rewrite it as

$$\mathrm{d}\phi = \frac{a}{\Delta}\left[(r^2+a^2)\varepsilon - a\mathscr{L}\right]\mathrm{d}\lambda + \frac{\mathscr{L}}{1-z^2}\mathrm{d}\lambda - a\varepsilon\,\mathrm{d}\lambda,$$

and replace $\mathrm{d}\lambda$ on the first and second terms on the right-hand side by $\mathrm{d}r$ and $\mathrm{d}z$ obtained from Eqs. (39) and (36), respectively. Doing so makes each term directly integrable, so that ϕ is described by

$$\phi(\lambda) = \phi_r(\lambda) + \phi_z(\lambda) - a\varepsilon\lambda, \tag{46}$$

where the subscript on the different functions on the right-hand side denote the integrals that originate them, and are defined by

$$\phi_r = a\frac{\left[(r_I^2+a^2)\varepsilon - a\mathscr{L}\right]\lambda}{(r_I - r_-)(r_I - r_+)} + \frac{a}{\sqrt{1-\varepsilon^2}}\times \\ \times\left[\frac{(r_-^2+a^2)\varepsilon - a\mathscr{L}}{\sqrt{\mathfrak{r}_{-4}\mathfrak{r}_{I-}^3}\,\mathfrak{r}_{+-}}\ln\left(\frac{2\sqrt{\mathfrak{r}_{-4}} + \lambda\,\mathfrak{r}_{I4}\sqrt{(1-\varepsilon^2)\mathfrak{r}_{I-}}}{2\sqrt{\mathfrak{r}_{-4}} + \lambda\,\mathfrak{r}_{I4}\sqrt{(1-\varepsilon^2)\mathfrak{r}_{I-}}}\right) + \right. \\ \left. + (r_+ \Longleftrightarrow r_-)\right], \tag{47}$$

$$\phi_z = \frac{\mathscr{L}}{z_2}\Pi(z_1^2; \xi_z(\lambda)|k_z^2), \tag{48}$$

where i) $\Pi(n;\varphi|k)$ is the incomplete elliptic integral of the third kind, ii) we defined $\mathfrak{r}_{ij} = r_i - r_j$ and iii) the double arrow symbol signifies the next term equals the previous with r_+ switched for r_- and vice-versa.

D. The Time Equation

The time dependence is solved in a similar fashion as the azimuthal one. We start from Eq. (37) and rewrite it as

$$\mathrm{d}t = \frac{r^2+a^2}{\Delta}\left[(r^2+a^2)\,\varepsilon - a\,\mathscr{L}\right]\mathrm{d}\lambda - \\ -a^2\,\varepsilon\,(1-z^2)\,\mathrm{d}\lambda + a\,\mathscr{L}\,\mathrm{d}\lambda, \tag{49}$$

and again replace $\mathrm{d}\lambda$ on the first and second terms on the right-hand side by $\mathrm{d}r$ and $\mathrm{d}z$ from Eqs. (39) and (36), respectively. Again, doing so makes each term directly integrable, giving

$$t(\lambda) = t_r(\lambda) + t_z(\lambda) + a\,\mathscr{L}\,\lambda, \tag{50}$$

where the functions t_r and t_z are

$$t_r = \frac{(r_I^2+a^2)\left[(r_I^2+a^2)\,\varepsilon - a\,\mathscr{L}\right]\lambda}{\mathfrak{r}_{I-}\,\mathfrak{r}_{I+}} + \frac{2\,\mathfrak{r}_{I4}^2\,\varepsilon\,\lambda}{4+(1-\varepsilon^2)\,\mathfrak{r}_{I4}^2\,\lambda^2} - \\ -\frac{r_4+3\,r_I+2\,(r_+ + r_-)}{\sqrt{1-\varepsilon^2}}\,\varepsilon\arctan\left(\frac{\mathfrak{r}_{I4}\,\lambda\sqrt{1-\varepsilon^2}}{2}\right) + \\ +\left[\frac{(r_-^2+a^2)[(r_-^2+a^2)\varepsilon - a\,\mathscr{L}]}{\mathfrak{r}_{+-}\sqrt{(1-\varepsilon^2)\,\mathfrak{r}_{I4}\,\mathfrak{r}_{I-}^3}}\times\right. \\ \times\ln\left(\frac{2\,\mathfrak{r}_{-4}+\mathfrak{r}_{I4}\,\lambda\,\sqrt{(1-\varepsilon^2)\,\mathfrak{r}_{I-}}}{2\,\mathfrak{r}_{-4}-\mathfrak{r}_{I4}\,\lambda\,\sqrt{(1-\varepsilon^2)\,\mathfrak{r}_{I-}}}\right) + \\ \left.+(r_+ \Longleftrightarrow r_-)\right], \tag{51}$$

$$t_z = \frac{\varepsilon}{1-\varepsilon^2}\left[(z_2^2 - a^2\,(1-\varepsilon^2))\,\lambda - z_2\,E(\xi_z(\lambda)|k_z^2)\right], \tag{52}$$

where $E(\varphi|m)$ is the incomplete elliptic integral of the second kind and $\mathfrak{r}_{ij}$ and the double arrow symbol are as before. The trajectory of the particle is shown in Fig. 1 and the horizontal projection of this trajectory is shown in Fig. 2. The particle rotates around the ring singularity, where it eventually falls. Upon reaching each event horizon, the particle spends what seems for an exterior observer to be an infinite amount of time before passing through, just as is verified for the Schwarzschild black hole.

IV. CONCLUSIONS

It is found that analytic solutions describing test particles falling from the ISSO can be obtained. This procedure shows the specific gauge choice, i.e., choice of coordinates, is a critical step and the solutions come in the form of elliptic functions. Thus, this work serves as an important stepping stone in understanding particle dynamics in rotating spacetimes. In particular, and more specifically, the methods used are expected to be characteristic to this type of system, so that applying them to other similar systems, such as compact object binaries, collision and collapse, should come naturally. We propose that the next line of focus should then be i) the study of more complex systems; and ii) the study of different coordinate systems and the advantages they bring is sutdying different physical phenomena.

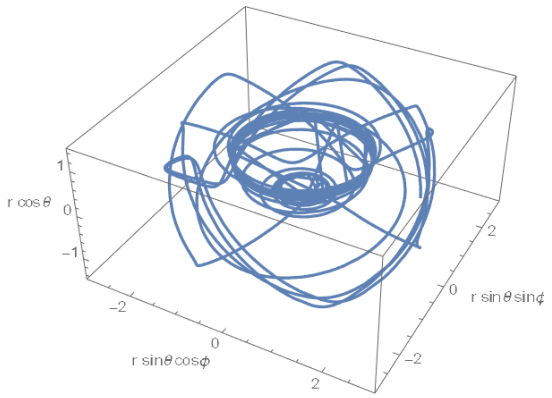

Fig. 1. Trajectory of a falling timelike particle, in (r,θ,ϕ) coordinates, and beginning fall from the ISSO with $(a, r_I) = (0.9, 2.6)$. After initiating fall, the particle reaches the outer and interior event horizons, r_+ and r_-, respectively, before reaching the ring singularity at the center.

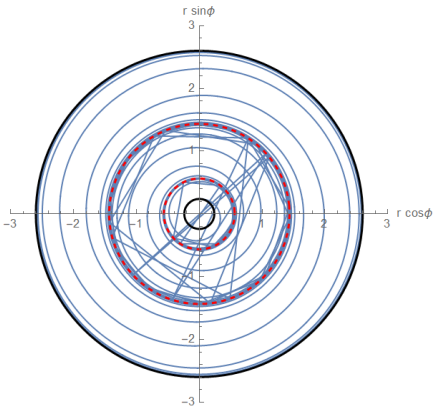

Fig. 2. Projection of the trajectory from Fig. 1 on the horizontal plane. The outer black circle is the ISSO, from which the particle begins fall, and the inner one is the ring singularity, where the trajectory ends. The red dashed outer and inner circles are the event horizons, r_+ and r_-, respectively. Here we see the relation with the event horizons, where an exterior observer sees the particle spend an infinite amount of time. The straight lines at the center are artifacts of computation due to insufficient resolution.

REFERENCES

[1] D. Silva, "Gravitational Collapse and Black Holes", MsC Thesis, IST-ULisboa, Lisbon, July 2020.

[2] R.d'Inverno, "Introducing Einstein's Relativity", Oxford University Press, Oxford, June 1992.

[3] R. P. Kerr, "Gravitational Field of a Spinning Mass as an Example of Algebraically Special Metrics", Phys. Rev. Lett. **11**, September 1963, 237–238.

[4] B. Carter, "Global Structureof the Kerr Family of Gravitational Fields", Phys. Rev. **174**, October 1968, 1559–1571.

[5] E. T. Newman et al., "Metric of a Rotating, Charged Mass", J. Math. Phys. **6**, June 1965, 918–919

[6] Y. Mino, "Perturbative Approach to an Orbital Evolution Around a Supermassive Black Hole", Phys. Rev. D **67**, April 2003, 084027.

[7] C. Dyson and M. van de Meent, "Kerr-fully Diving into the Abyss: Analytic Solutions to Plunging Geodesics in Kerr", February 2023, arXiv:2302.03704

[8] M. Abramowitz and I. A. Stegun, "Handbook of Mathematical Functions", Dover Books on Mathematics, New York, June 1965

[9] A. J. Brizard, "A primer on elliptic functions with applications in classical mechanics", November 2007, arXiv:0711.4064v1

Spectra of interference between harmonic components due to group velocity mismatch

G. Vaz[1], H.Pires[1], G. Williams[1], M. Hussain[2], M. Fajardo[1] and G. Figueira[1]

***Abstract*— Using Sellmeier equations, we study interference patterns in the spectra of harmonics generated by the nonlinear interaction between ultrashort laser pulses at 3 μm and solid samples. For most cases, the measured fringe spacings point to the formation of two harmonic components that propagate with different group velocities, even if they have the same frequency. Potential applications are the fine control of temporal separation and interference spectra by careful sample selection.**

I. INTRODUCTION

The generation of low-order harmonics is one of the most well-established applications of the nonlinear response of materials to high-intensity laser pulses. The very birth of the field of nonlinear optics can be traced to the first observation of Second Harmonic (SH) generation by Franken *et al* in 1961 [1]. SH is related to second order (perturbative) term of the response of the medium's polarization, $P(E) = \epsilon_0 \sum_{i=1}^{\infty} \chi^{(i)} E^i$, to the electric field, E, where ϵ_0 is the vacuum permittivity and $\chi^{(i)}$ the i-th order electric susceptibility. Therefore it is no surprise that $\chi^{(2)}$ phenomena are among the best understood in the field thanks to its intensive study. In 1988 a new harmonic generation method in gases was observed by Ferray *et al* [2], which was marked by harmonics of higher orders and the formation of a plateau in intensity, unlike the perturbative case where the harmonic yield diminishes with the increasing order. This phenomenon would later become known as High-Harmonic Generation (HHG) and its extension to solid samples was only possible after the development of high-power lasers in the mid-infrared, first observed by Ghimire *et al* [3] in 2011 employing $\sim 3.2 - 3.7$ μm pulses.

Most studies of SH focus on phase-matched conditions, however, in non-ideal matching conditions it has been observed the generation of two separate forward-propagating SHs, e.g. [4], [5], [6]. These are marked by a Group Velocity Mismatch (GVM), where one of the components travels with a group velocity associated with its wavelength while the other with the same group velocity as the fundamental.

Although mainly studied for SH, this phenomenon is not exclusive to $\chi^{(2)}$ as it was observed by Aközbek *et al* [7] when they generated Third Harmonics (THs) ($\chi^{(3)}$) during filamentation of laser pulses in air. In this work, they observed what they called a "... two-color filamentation effect... due to a nonlinear phase-locking mechanism which couples the fundamental and the TH pulse together, with constant phase difference inside the filament". These phase locking mechanisms for both $\chi^{(2)}$ and $\chi^{(3)}$ were validated by Roppo *et al* [8] by means of numerical simulation. In their work they observed the formation of 3 harmonic components at the surface of the sample: i) a small backward (reflected) component, ii) a free forward (transmitted) component which separates from the fundamental, and iii) a forward phase-locked component trapped by it.

More recently, Garejev *et al* [9] observed two third harmonic components in a solid sample of CaF_2. They used 1.98 μm laser pulses to generate harmonics in a wedge-shaped CaF_2 sample so they could vary the propagation length within the medium. For larger propagation lengths ($\sim$ 1 mm) the spectrum would possess spectral fringes, due to interference between the harmonic components, while with smaller lengths the expected fringe spacing would exceed the Full Width At Half Haximum (FWHM) of the spectrum and therefore no fringes were observed. Yet further studies with other materials or higher harmonics are so far lacking.

In this work, we study the spectral fringes of low-order harmonics (3rd and 5th) generated in transmission by the propagation of short mid-infrared laser pulses through standardized transmission windows. For each harmonic, we calculate the fringe spacing both experimentally and theoretically with the aid of Sellmeier equations.

II. METHODS

In this section, we proceed to explain the methods used to acquire and treat the data in this work.

A. Experimental setup

We used a Yb:YAG laser (Amphos2000, AMPHOS) delivering 0.75 mJ, 1 ps pulses at 100 kHz and central wavelength of 1.03 μm to pump an Optical Parametric Chirped-Pulse Amplification (OPCPA) system (Starzz, FASTLITE). The output of the latter consists of 3 μm, 40 fs pulses with a repetition rate of 100 kHz.

For the generation of the harmonics we placed our standard samples, see Tab. I, in a rotation mount at the focus of the OPCPA, allowing us to orientate the samples around its axis, see Fig. 1. At the focus we obtained up to $\sim$50 TW/cm^2 in peak intensity.

After generation, the harmonics were then collimated into a prism separating the different wavelengths in space so that they could be measured separately using an ultraviolet optical fiber connected to a spectrometer (FLEX-STD-UV-Vis-NIR, SARSPEC). The separation was required to block

[1] Group of Lasers and Plasmas/Instituto de Plasmas e Fusão Nuclear-Laboratório Associado, Instituto Superior Técnico, Universidade de Lisboa, 1049-001 Lisboa, Portugal

[2] Extreme Light Laboratory, Department of Physics and Astronomy, University of Nebraska-Lincoln, Lincoln, Nebraska 68588, USA

Corresponding author: goncalovaz98@tecnico.ulisboa.pt

the fundamental as the mid-infrared light could damage the optical fiber in use. A complete description of the experimental setup and procedure can be found in [10].

TABLE I: Samples used in this work.

Material	Thickness (mm)
CaF_2	1
	3
Fused Silica	5
LiF	3
Sapphire	1 (unknown cut- A, M or R)
	2 (C-cut)

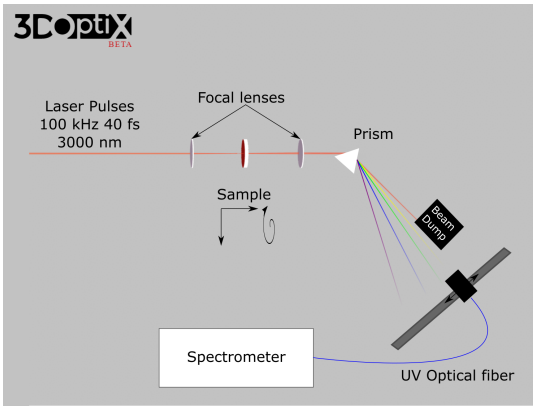

Fig. 1: Simplified experimental setup where short 3 μm laser pulses are focused in a solid sample to generate harmonics. These are then collimated into a prism which separates them while the fundamental is sent to a beam dump. Each harmonic is then measured separately using a movable optical fiber coupling connected to a spectrometer. A full version can be consulted in [10].

B. Data treatment

For each of the harmonics, we used the spectrum obtained when the orientation of the sample was set to give the maximum number of integrated counts in our spectrometer, for a better Signal-to-Noise Ratio (SNR). All spectra were then fitted to a Gaussian to extract the central wavelength of the harmonic, λ_H, allowing us to calculate an expected/theoretical fringe spacing as [11]:

$$\Delta\lambda_{theo} = \frac{\lambda_H^2}{d\left(n_g(\lambda_0) - n_g(\lambda_H)\right)}, \quad (1)$$

where λ_0 =3 μm is the central wavelength of the fundamental, d is the sample's thickness, and $n_g(\lambda) = n(\lambda) - \lambda\frac{dn(\lambda)}{d\lambda}$ is the group index of the sample for the wavelength λ. The refractive index of the medium, $n(\lambda)$, was obtained from the Sellmeier equations of these media, see appendix.

The experimental spectral fringe, $\Delta\lambda$, was defined as the maximum separation between consecutive peaks, we took this approach instead of a center of mass because in some cases we were expecting fringe spacings of a few nanometers, e.g. Fig. 4. To help reduce the effect of noisy peaks we also calculated $\Delta\lambda$ from spectra smoothed by a Savitzky-Golay filter[1].

III. RESULTS AND DISCUSSION

In general, we obtained a good agreement with the theory, in particular for spectra that demonstrated prominent fringes, see Fig. 2, pointing to the existence of two harmonics components with a GVM as it was observed by the teams of Aközbek [7] and Garejev [9]. The small deviation could be associated with the usage of an incorrect wavelength, experimental uncertainty, and possible discrepancies of the refractive index from the Sellmeier equation.

It is important to notice that for the 1 mm Sapphire sample the positions of the fringes change with the orientation of the sample while the spacing does not change significantly. This might be related to the birefringence of the sapphire for this cut. From previous works, we could conclude that the cut should be either A, M, or R-cut (birefringent) while the 2 mm Sapphire is C-cut ("zero degree", non-birefringent). This could also be the cause of the higher deviation from theory of the results in Fig. 2b.

As for the samples that did not result in visible interference, for most cases this could be related to one of two situations:

1) As mentioned in section I if the GVM is too small the fringes would be greater than the FWHM of the harmonic, therefore not observable. See e.g. Fig. 3.
2) In opposition the mismatch can be of such a magnitude that the spectral fringes are too close to be resolved by the spectrometer. See e.g. Fig. 4.

In almost all instances we could not observe spectral fringes in harmonics higher than 3rd either due to the low intensity of these harmonics (low SNR) or because the fringes would not be measurable for our samples and wavelengths, see e.g. Fig. 5. As such we could not verify if the formation of this double component harmonics can occur for nonlinearities above $\chi^{(3)}$. In future works, we would need to select samples with the right thickness and GVM to generate measurable spectral fringes at these wavelengths.

However, there were two particular cases where we observed interference patterns in 5th harmonics that were not related to the difference in group velocities, see Fig. 6. One possibility is that these interference patterns are instead consequence, still, of two harmonic components but in this case, one results from the short trajectory of the electrons in the conduction band during HHG, while the other (generated later) from the long trajectory as observed by Kim *et al* [12] in the 7th harmonic of an 800 nm laser, generated in a 430 μm A-cut Sapphire. To verify this possibility we would need numerical simulations similar to the ones performed by them. In the case of Fig.6a, it could be argued that the difference

[1]Corresponding to the function *savgol_filter* in the *scipy.signal* library of *Python*.

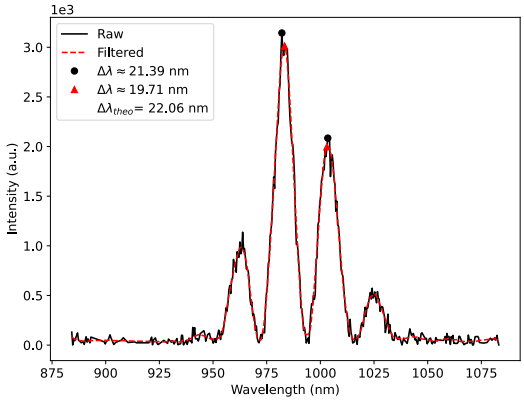

(a) LiF sample.

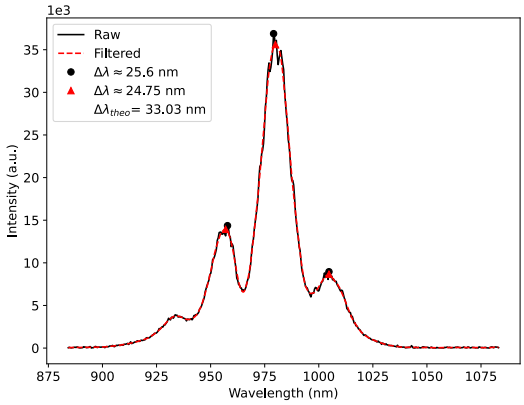

(b) 1 mm sapphire sample.

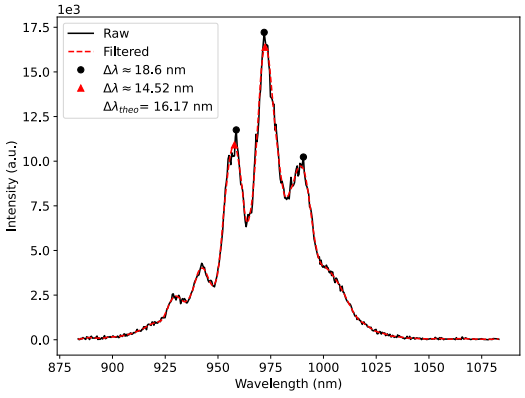

(c) 2 mm sapphire sample.

Fig. 2: TH spectra displaying prominent fringes and demonstrating good agreement between $\Delta\lambda$ and $\Delta\lambda_{theo}$. For the cases of (a) and (c) the positions of the peaks are orientation independent, which is not the case for (b) possibly due to the cut of this sapphire sample. The latter could also explain the higher deviation from theory of the fringe spacing.

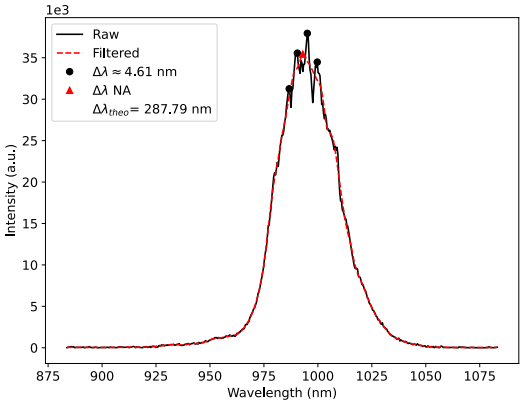

Fig. 3: Example of TH spectra where the fringe spacing exceeds the FWHM, generated in a 1 mm CaF_2 sample. As we can see in the filtered data we only have one peak and it is not possible to calculate a fringe spacing (NA- Not Applicable). The raw data presents some peaks but are likely related to noise.

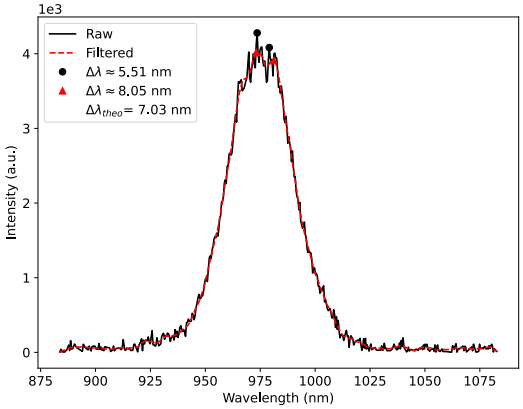

Fig. 4: Example of TH spectra where the fringe spacing is too small for our spectrometer to resolve the separate peaks, generated in a 5 mm Fused Silica sample. Although we can still measure a “fringe spacing" (possibly from noise) close to the theory we cannot observe any fringes similar to Fig. 2.

between the experiment and the theoretical prediction by GVM is still within expectation, however, taking into account that this is a 5th harmonic and we might have the competing process of HHG, we cannot infer for sure without simulation.

IV. CONCLUSIONS

In this work, we studied the spectral fringes observed in harmonic generation spectra. For 3rd harmonic these were associated with the generation of two harmonic components, at the entrance of the sample, traveling at different group velocities. In some cases, we could not observe these fringes either because the spacing was too small to be resolved by

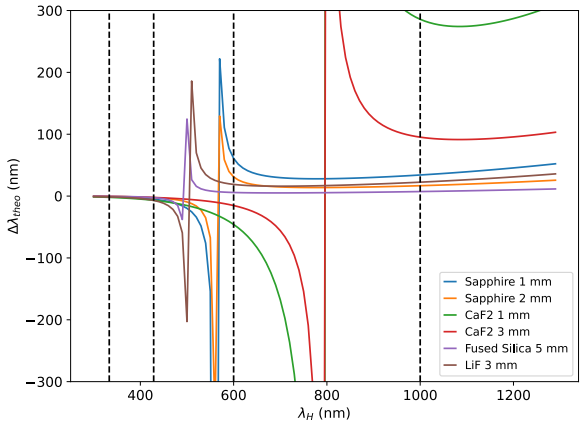

Fig. 5: Expected spectral fringes in function of the harmonic wavelength calculated from Eq. 1 for all samples in Tab. I. The black dashed lines correspond to the expected harmonic wavelength from the 3rd to the 9th (from right to left) assuming λ_0 =3 μm.

the spectrometer or was too big (above the FWHM of the harmonic) to be observable.

This was the case for most 5th harmonics and so we are not able to test the existence of these two components for higher orders of $\chi^{(n)}$. To test this we would need to carefully select different samples (thickness and GVM) to assure the generation of visible fringes.

For two specific cases, the fringe spacing was observable but not within expectations. One possibility is that instead of the GVM the source of the temporal separation is the difference in the trajectory of the electrons during the HHG process. The verification of this would require numerical simulation as discussed in [12].

The observation of these fringes indicates that we could shape our harmonic spectrum by changing either the material or its thickness. In particular, we could use wedge samples, as in the case of [9], placed in a translation mount allowing to diminish or increase the fringe spacing/harmonic separation through positioning.

ACKNOWLEDGMENT

This work was supported by Fundação para a Ciência e a Tecnologia and Laserlab Europe.

APPENDIX

The Sellmeier equations used in this work are specified through Eq. A.1 and its coefficients in Tab. A.1. These equations were taken from the `refractiveindex.info` database.

$$n(\lambda) = \sqrt{B_0 + \frac{B_1 \cdot \lambda^2}{\lambda^2 - C_1^2} + \frac{B_2 \cdot \lambda^2}{\lambda^2 - C_2^2} + \frac{B_3 \cdot \lambda^2}{\lambda^2 - C_3^2}} \quad \text{(A.1)}$$

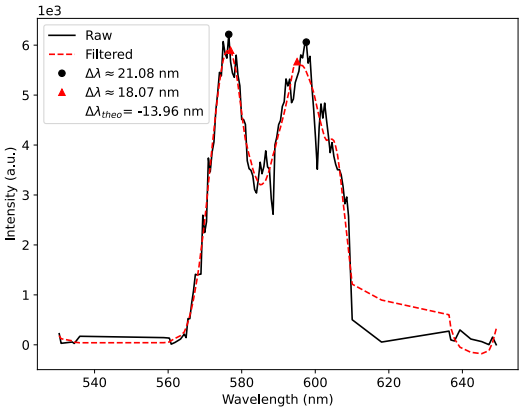

(a) 3 mm CaF_2 sample.

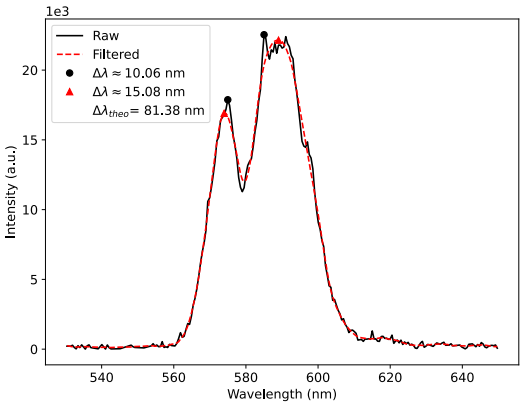

(b) 1 mm sapphire sample.

Fig. 6: Cases of 5th harmonic spectra which presented fringe spacings that were not within expectations for the respective sample and propagation length.

TABLE A.1: Coefficients of the Sellmeier equations. B_i is adimentional and C_i is in micrometer.

	CaF_2	Fused Silica	LiF	Sapphire	
				ordinary ray	extraordinary ray
B_0	1.33973	1	1	1	1
B_1	0.69913	0.6961663	0.92549	1.4313493	1.5039759
C_1	0.09374	0.0684043	0.07376	0.0726631	0.0740288
B_2	0.11994	0.4079426	6.96747	0.65054713	0.55069141
C_2	21.18	0.1162414	32.79	0.1193242	0.1216529
B_3	4.35181	0.8974794	-	5.3414021	6.5927379
C_3	38.46	9.896161	-	18.028251	20.072248

REFERENCES

[1] P. A. Franken, A. E. Hill, C. W. Peters, and G. Weinreich, "Generation of optical harmonics," *Physical Review Letters*, vol. 7, pp. 118–119, 8 1961. [Online]. Available: https://link.aps.org/doi/10.1103/PhysRevLett.7.118

[2] M. Ferray, A. L'Huillier, X. F. Li, L. A. Lompre, G. Mainfray, and C. Manus, "Multiple-harmonic conversion of 1064 nm radiation in rare gases," *Journal of Physics B: Atomic, Molecular and Optical Physics*, vol. 21, pp. L31–L35, 2 1988. [Online]. Available: https://iopscience.iop.org/article/10.1088/0953-4075/21/3/001

[3] S. Ghimire, A. D. DiChiara, E. Sistrunk, P. Agostini, L. F. DiMauro, and D. A. Reis, "Observation of high-order harmonic generation in a bulk crystal," *Nature Physics*, vol. 7, pp. 138–141, 2 2011. [Online]. Available: http://www.nature.com/articles/nphys1847

[4] S. L. Shapiro, "Second harmonic generation in $LiNbO_3$ by picosecond pulses," *Applied Physics Letters*, vol. 13, pp. 19–21, 7 1968. [Online]. Available: https://pubs.aip.org/aip/apl/article/13/1/19-21/41123

[5] L. D. Noordam, H. J. Bakker, M. P. de Boer, and H. B. van Linden van den Heuvell, "Second-harmonic generation of femtosecond pulses: observation of phase-mismatch effects," *Optics Letters*, vol. 15, p. 1464, 12 1990. [Online]. Available: https://opg.optica.org/abstract.cfm?URI=ol-15-24-1464

[6] R. M. Rassoul, A. Ivanov, E. Freysz, A. Ducasse, and F. Hache, "Second-harmonic generation under phase-velocity and group-velocity mismatch: influence of cascading self-phase and cross-phase modulation," *Optics Letters*, vol. 22, p. 268, 3 1997. [Online]. Available: https://opg.optica.org/abstract.cfm?URI=ol-22-5-268

[7] N. Aközbek, A. Iwasaki, A. Becker, M. Scalora, S. L. Chin, and C. M. Bowden, "Third-harmonic generation and self-channeling in air using high-power femtosecond laser pulses," *Physical Review Letters*, vol. 89, p. 143901, 9 2002. [Online]. Available: https://journals.aps.org/prl/abstract/10.1103/PhysRevLett.89.143901https://link.aps.org/doi/10.1103/PhysRevLett.89.143901

[8] V. Roppo, M. Centini, C. Sibilia, M. Bertolotti, D. de Ceglia, M. Scalora, N. Akozbek, M. J. Bloemer, J. W. Haus, O. G. Kosareva, and V. P. Kandidov, "Role of phase matching in pulsed second-harmonic generation: Walk-off and phase-locked twin pulses in negative-index media," *Physical Review A*, vol. 76, p. 033829, 9 2007. [Online]. Available: https://link.aps.org/doi/10.1103/PhysRevA.76.033829

[9] N. Garejev, I. Gražulevičiūtė, D. Majus, G. Tamošauskas, V. Jukna, A. Couairon, and A. Dubietis, "Third- and fifth-harmonic generation in transparent solids with few-optical-cycle midinfrared pulses," *Physical Review A*, vol. 89, p. 033846, 3 2014. [Online]. Available: https://link.aps.org/doi/10.1103/PhysRevA.89.033846

[10] G. Vaz, "Nonlinear optics with ultrashort mid-infrared laser pulses," Master's thesis, Instituto Superior Técnico, Universidade de Lisboa, 2021. [Online]. Available: https://fenix.tecnico.ulisboa.pt/cursos/meft/dissertacao/1128253548922926

[11] D. Franz, A. Klisnick, P. Jan, L. Rapporteur, P. Angela, V. Examinatrice, F. Druon, and H. Merdji, "High harmonic generation in crystals assisted by local field enhancement in nanostructures." [Online]. Available: https://theses.hal.science/tel-01830832

[12] Y. W. Kim, T.-J. Shao, H. Kim, S. Han, S. Kim, M. Ciappina, X.-B. Bian, and S.-W. Kim, "Spectral interference in high harmonic generation from solids," *ACS Photonics*, vol. 6, pp. 851–857, 4 2019. [Online]. Available: https://pubs.acs.org/doi/10.1021/acsphotonics.9b00019

How X-ray free electron lasers have enabled a new perspective on high energy density plasma physics*

Lucas Ansia[1], Gareth Williams[1] and Marta Fajardo[1]

***Abstract*— In this review, we explore how the advent of X-ray free-electron lasers (XFELs) has revolutionized the study of warm dense matter (WDM) by enabling the creation of high-quality samples in the laboratory. One of the most important results has been the direct measurement of the continuum depression, which has allowed for a more accurate characterization of the plasma state. Additionally, collisional radiative models together with novel experimental results have been used to characterize the evolution of WDM on the femtosecond timescale, allowing an unprecedented understanding of such extreme conditions.**

I. INTRODUCTION

Over the past two decades, X-ray free-electron lasers (XFELs) have undergone significant progress, resulting in peak brightness in the XUV and X-ray regions that were previously only attainable in the optical and infrared ranges. These lasers have achieved intensities greater than 10^{18} W/cm^2 [1], which has opened up new possibilities in high energy density science, a field highly related to many disciplines such as astrophysics [2] and inertial fusion [3].

High-density matter (HDM) refers to the study of matter under extreme conditions, such as high pressure, radiation, and temperature, which exceed 10^{11} J/m^3. Warm dense matter (WDM) is usually referred to as the state lying between solid and plasma state when the degenerate effects are predominant, i. e. strongly coupled regime.

Studying matter under extreme conditions presents a challenge in itself. The primary approach to recreate these states is by focusing high-energy lasers and particle beams into solid samples. However, non-uniformities and a decay time in the range of femto to picoseconds create several difficulties in measuring fundamental phenomena in these plasmas.

With the development of XFELs, it has become possible to create samples with larger volumes, greater uniformity, and well-defined properties such as temperature and density. This has opened up a new realm of experiments dedicated to validating existing codes and measuring fundamental parameters in HDM. Typical temperature-density conditions achievable with XFELs when irradiating solid targets are $100 - 200$ eV and 10^{24} cm^{-3} [4].

XFEL technology has allowed for reliable measurement of continuum lowering, which refers to the reduction in the energy required to ionize a material under high-density conditions. This phenomenon occurs due to the screening of neighbouring ions and free electrons.

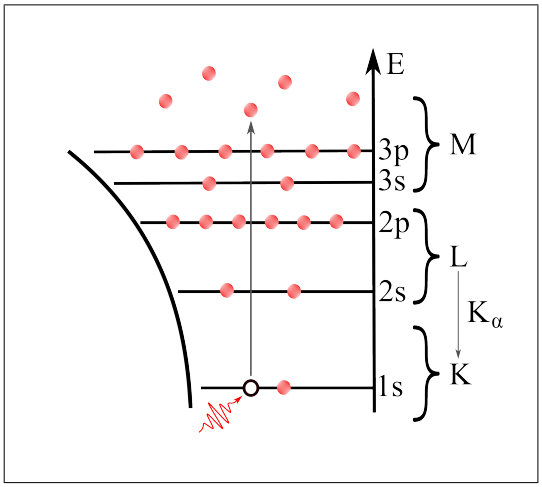

Fig. 1. Schematic representation of photoionization process, where an incoming photon ejects a bound electron to the continuum. In the right is pointed the usual spectroscopy notation for the atomic level and $K_{|\alpha}$ transition.

Spectroscopy is the most commonly used diagnostic technique as it allows for the measurement of plasma evolution and can be replicated using collisional radioactive models. These measurements enable the characterization of ion/electron dynamics on a femtosecond scale in unprecedented experimental conditions.

The paper is structured as follows. First, we present the fundamentals of XFELs and their advantages in order to create WDM samples. Measurements of continuum lowering and its implication are revisited in the second section. We conclude with an introduction to collisional radioactive models together with some exemplifying results.

II. WARM DENSE MATTER

A. XFEL fundamentals

XFELs are capable of producing high-power and coherent radiation in regimes that are not accessible with conventional lasers and synchrotron radiation sources. The basic idea behind them involves first accelerating a highly compressed bunch of electrons to relativistic velocities.

The electron pulse then passes through an undulator, which is a periodic structure with alternating magnetic fields. An oscillating trajectory is induced, emitting highly collimated

*This work was supported by Fundação para a Ciência e a Tecnologia (FCT) under the Advanced Programme in Plasma Science and Engineering (APPLAuSE) PhD program.

[1]Experimental Group of laser and plasmas (X-GoLP), Instituto de Plasmas e Fusão Nuclear, Instituto Superior Técnico, Universidade de Lisboa, Av. Rovisco Pais 1, 1049-001 Lisboa, Portugal. lucas.ansia.fernandez@tecnico.ulisboa.pt

radiation in the undulator direction. Due to the periodicity of the undulator, there is a resonant frequency λ_r for the emitted photons [5]:

$$\lambda_r = \frac{\lambda_u}{2\gamma_0^2}(1 + \frac{K_0^2}{2}). \quad (1)$$

Here, λ_u is the undulator period, K_0 is the undulator characteristic parameter [6], and γ_0 is the usual Lorentz factor. For an undulator parameter on the order of magnitude of unity, the emission frequency is a factor of γ_0^{-2} lower than the undulator period.

At XFELs, the coherence of the emitted pulse is achieved via the Self Amplified Spontaneous Emission (SASE) process, which arises from the collective behaviour of electrons and their interaction with the emitted radiation. As electrons travel through the undulator they are grouped into micro-bunches leading to in-phase radiation emission as demonstrated by Saldin and Kondratenko in 1980 [7]. Non-destructive interference is created in the emission process, allowing for the achievement of massive intensities.

B. XFEL-matter interaction and Sample evolution

The main absorption process while irradiating a solid sample is the photo-ionization of the inner shells. A scheme representing this process along with the usually employed spectroscopy notation is shown in Fig. 1. The lower cross-section of this interaction (in comparison with the main absorption process in the infrared-visible) is responsible for the high level of sample uniformity achievable using XFELs.

After the laser arrival, unstable atom configurations are created. Lower energy holes are filled mainly via Auger emission and photo de-excitation. The relative strength of both processes depends on the atomic number (low Z materials present a strong preference for the non-radioactive process). Auger emissions create highly energetic electrons, which transfer the deposited laser energy to the electrons in the continuum or the ion lattice.

Electronic transitions, for example, K_α for the L to K transition (Fig. 1), lead to the characteristic XFEL emission spectra. Fig. 2 shows the results obtained by Vinko et al. [8] from a 1.0-mm-thick aluminium (Al) foil from incident photon energies between 1560-1820 eV. As the atom starts to ionize, the reduced screening leads to a tighter bound of the remaining electrons, increasing the energy for both ionising the inner shells (K-edge) and for the emitted radiation in the K-L transition. These higher energy transitions are often called satellites. Note that Roman numbers are used to represent the different ion charge states, being 3+ the ground state for Al (3 M-shell, third valence band, electrons are free-electrons like).

The XFEL energy can be tuned in order to only be able to ionize the main transition. This is clear for the aluminium spectra as in the minimum energy only the 4+ line is observed and constitutes a unique measure of the potential depression. Nonetheless, some emission lines a priory are forbidden, since the incident photon energy lower than the K-edge, is observed. In this case, collisional ionization of an already photo-ionized state is the alternative path to reach these higher satellites, constituting a measure of the collisional rate between electrons and ions, as we will see in the modelling section. The other possible path, represented as a white dotted line, is the resonant absorption, where a K-shell electron is promoted to an L-shell vacant.

III. CONTINUUM LOWERING PHENOMENA

As it was said in the introduction, the multi-body process arising in warm dense plasmas leads to a decrease in the continuum (minimum required energy to photo-ionize a specific shell). This effect is also known as ionization potential depression (IPD). It plays a key role as it limits the available bound states in the system corresponding to strong changes in the thermodynamic properties such as equations of states, opacity and emissivity, all fundamental for hydrodynamic simulations [9], [10].

Several models have been suggested in the literature to predict this behaviour. Nonetheless, the lack of experimental results in such an environment limited potential validations. XFEL photon energy is tunable as it depends on the undulator periodicity and the strength of the magnetic field. Scanning the emission K_α spectra for different energy allows us to infer the minimum energy needed to photo-ionize the inner shell, as only above it is possible to create the hole needed in the K-shell. This constitutes a unique technique to measure the IPD, for a well know temperature and density, of WDM and HDM.

Even more, because of the clear footprint of different satellites in the emission spectra, it is able to study how IPD varies as a function of the ionization. Fig. 3 shows the emission spectra obtained by Ciricosta et al. [11] at the LCLS for a magnesium target, along with a specific emission line for different charge states represented horizontally for clarity.

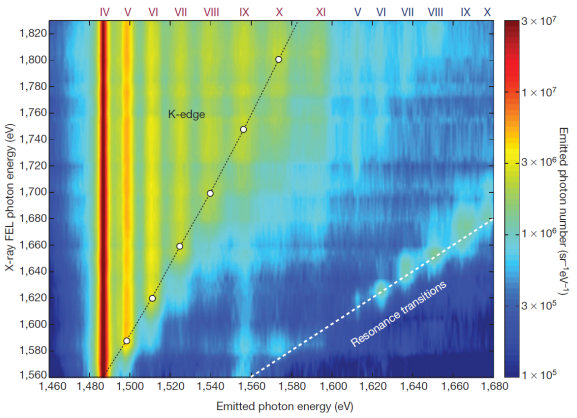

Fig. 2. K_α emission spectra as a function of incident photon energy in a logarithmic colour scale. Roman numbers represent the ion charge state (red for single K-hole and blue for double). Resonance K-L photo-absorption is highlighted in the dotted white line. K-edge line was calculated via a modified version of the SP model [8].

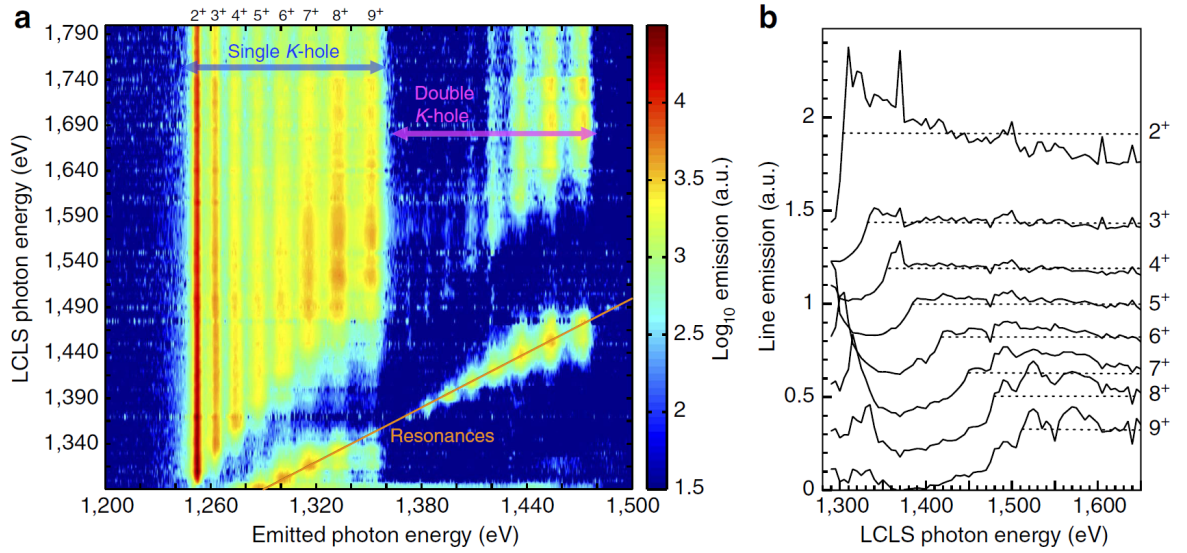

Fig. 3. a) K_α spectra as a function of the incident photon energy and b) emission lines for different charge states. Discontinuous lines are a visual guide to see the plateau and identify the K-edge [11].

Dotted lines were added in order to remark where the K-edge is observed for each ionization stage.

On the modelling side, the Stewart and Pyatt (SP) model [12], an interpolation between the low-temperature Debye-Huckel (DH) theory[13] and the Ion sphere model[14], was the most used approach to account for this phenomenon because of its agreement with laser shock experiments accounted at ORION [15]. However, results from XFEL favoured the older Ecker-Kröll (EK) model [16] as the SP tends to underestimate the IPD [17].

Each model agreeing with different results without a clear physical meaning remark the necessity of more robust models to take into account the IPD. Lately, studies employing first-principle density functional theory (DFT) calculations have emerged as an alternative [18], [19]. Even so, finite temperature DFT in the WDM regime is still a developing field and the required computational resources make it difficult to implement in fully atomic/collisional radioactive codes.

IV. COLLISIONAL-RADIOACTIVE CODES

In the conditions of the experiments, non-local thermodynamic equilibrium (N-LTE) can be assumed. This is mainly because of the ionic populations produced by the incident radiation (not in equilibrium with the system). Even if that collision rate is high, local thermodynamic equilibrium (LTE) can underestimate the population of higher ionize states, specifically in the first femtosecond on interaction while the lattice is still cold. The usual approach to simulate the full relaxation are the so-called collisional radioactive models (CRM) [20].

The simplest CRM codes assume a vast number of ionic states interacting with a free electron gas in thermal equilibrium. For each ion, atomic levels and transition rates for all relevant atomic processes are calculated. Time resolve evolution is obtained by solving the set of coupled differential rate equations,

$$\frac{dn_i}{dt} = \sum_{i \neq j}^{N} n_j R_{ji} - n_i R_i, \tag{2}$$

where n_i represents the density of each ionic state, R_{ji} is the total rate of creation of level i and R_i is the total rate of destruction of the same level. In order to calculate the atomic levels isolated atom approximations are commonly used together with an IPD model (EK is employed for XFEL experiments as stated above). The high number of possible states is not always computationally manageable, so energy level super-configurations (SC)[21], [22] are used. Rates are calculated by making use of relativistic levels obtained via detailed atomic codes such as the Flexible Atomic Code (FAC) [23] or HULLAC [24], and then averaged into each atomic shell as follows,

$$R_{\Xi \to \Xi'} = \frac{\sum_{i \in \Xi} \sum_{j \in \Xi'} g_i \exp(-\frac{E_i}{kT_e}) R_{ij}}{\sum_{i \in \Xi} g_i \exp(-\frac{E_i}{kT_e})}, \tag{3}$$

Where Ξ and Ξ' are the initial and final SC and i, j run all over the possible states within the configurations.

Ciricosta et al. [25] studied the evolution of a 1 μm Al foil, irradiated with photon energies between 1460 and 1830 eV at peak intensities of 10^{17} W/cm^2. Results were obtained

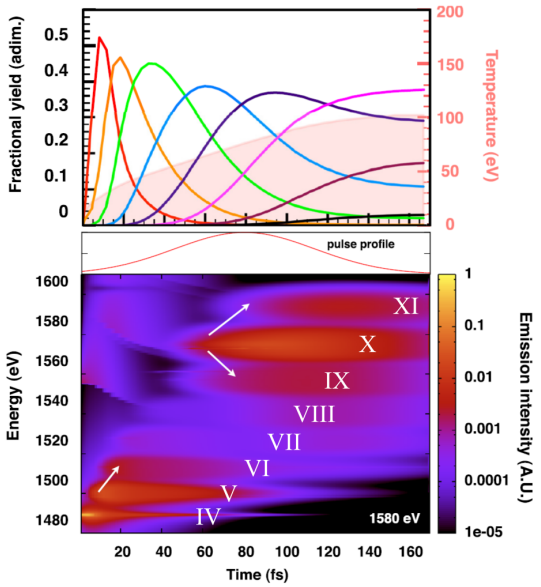

Fig. 4. Top, charge state and temperature evolution as a function of time. Bottom, emission spectra also as a function of time. White roman number represents the charge states that are responsible for such lines. White arrows remark the expected collisional ionization effects [25].

using the SCFLY [26] code, a CRM model based on super configurations. Fig. 4 shows the charge states, temperature and emission spectra as a function of time for an incident 1580 eV photon. For that specific energy, only the V and VI satellites can be directly ionized. Nevertheless, resonant absorption (it can be seen from the fact that the emission is at the same energy $\sim$ 1580) from a K-shell promoting to the L-shell leads to X-ion fluoresce. Collisional ionization triggers weaker emission in the ions VI, IX and XI.

This weaker emission is highly dependent on electron-ion coupling. Q. Y. van den Berg et al. [27] resonantly pumped the 1s - 2p transitions in order to study the off-resonance spectra and measure the collisional ionization cross-section. It was concluded that several up-to-date models were underestimating the collision rate for such extreme conditions, after introducing them into the SCFLY code and observing a lower emission intensity.

More complex effects have been developed in the last years to better understand plasma evolution. Electrons in the continuum have been modelled via the Fokker-Planck formalism to take into account non-thermal effects and determine whether or not is possible to assume an instant thermalization [28], [29]. Also, degeneracy effects have been studied including Pauli blocking in the transition rates calculations and considering Fermi Dirac statistics for the free electrons gas [30], [31].

V. CONCLUSIONS

High energy density regimes are now achievable thanks to the advent of X-ray free-electron lasers in the last few years. The measured spectra while pumping a solid to hundreds eV contain footprints of the system evolution during the heating/relaxation times.

The main XFEL-matter interaction allows establishing a unique measure of the ionization potential depression at the WDM regime, pointing to a poor agreement with the most commonly used analytical models.

Simulations employing collisional radioactive models have brought new possibilities, together with experimental results, to measure femtosecond dynamic as the ionic yield or collisional effect in Warm Dense Matter.

ACKNOWLEDGMENT

This work was supported by FCT (Portugal)—Foundation for Science and Technology under the project UID/50010/2020 and Grant No. UI/BD/153734/2022.

REFERENCES

[1] M. V. Kovalchuk and A. E. Blagov. “European X-ray Free-Electron Laser”. In: Crystallography Reports 67.5 (Sept. 2022), pp. 631–675.
[2] J. Daligault and S. Gupta. “Electron-ion scattering in dense multi-component plasmas: application to the outer crust of an accreting neutron star”. In: The Astrophysical Journal 703.1 (Sept. 2009), pp. 994–1011.
[3] A. B. Zylstra, O. A. Hurricane, D. A. Callahan, A. L. Kritcher, et al. “Burning plasma achieved in inertial fusion”. In: Nature 601.7894 (Jan. 2022), pp. 542–548.
[4] Byoung Cho. “X-ray Spectroscopies of High Energy Density Matter Created with X-ray Free Electron Lasers”. In: Applied Sciences 9 (Nov. 2019), p. 4812.
[5] Sandor Varro. “Free Electron Lasers”. Rijeka: IntechOpen, Mar. 2012.
[6] Zhirong Huang and Kwang-Je Kim. “Review of x-ray free-electron laser theory”. In: Physical Review Special Topics - Accelerators and Beams 10.3 (Mar. 2007).
[7] A. M. Kondratenko and E. L. Saldin. “Generating of coherent radiation by a relativistic electron beam on an undulator”. In: Part. Accel. 10 (1980), pp. 207–216.
[8] S. M. Vinko, O. Ciricosta, B. I. Cho, K. Engelhorn, et al. “Creation and diagnosis of a solid-density plasma with an X-ray free-electron laser”. In: Nature 482.7383 (Jan. 2012), pp. 59–62.
[9] S. X. Hu, B. Militzer, V. N. Goncharov, and S. Skupsky. “First-principles equation-of-state table of deuterium for inertial confinement fusion applications”. In: Physical Review B 84.22 (Dec. 2011).
[10] S. X. Hu, L. A. Collins, V. N. Goncharov, T. R. Boehly, et al. “First-principles opacity table of warm dense deuterium for inertial-confinement-fusion applications”. In: Physical Review E 90.3 (Sept. 2014).
[11] O. Ciricosta, S. M. Vinko, B. Barbrel, D. S. Rackstraw, et al. “Measurements of continuum lowering in solid-density plasmas created from elements and compounds”. In: Nature Communications 7.1 (May 2016).
[12] John C. Stewart and Jr. Pyatt Kedar D. “Lowering of Ionization Potentials in Plasmas”. In: The Astrophysical Journal 144 (June 1966), p. 1203.
[13] H. R. Griem. “Plasma Spectroscopy”. New York: McGraw-Hill, 1964.
[14] G.B. Zimmerman and R.M. More. “Pressure ionization in laser-fusion target simulation”. In: Journal of Quantitative Spectroscopy and Radiative Transfer 23.5 (May 1980), pp. 517–522.
[15] D. J. Hoarty, P. Allan, S. F. James, C. R. D. Brown, et al. “Observations of the Effect of Ionization-Potential Depression in Hot Dense Plasma”. In: Physical Review Letters 110.26 (June 2013).
[16] G. Ecker and W. Kröll. “Lowering of the Ionization Energy for a Plasma in Thermodynamic Equilibrium”. In: Physics of Fluids 6.1 (1963), p. 62.

[17] O. Ciricosta, S. M. Vinko, H.-K. Chung, B.-I. Cho, et al. “Direct Measurements of the Ionization Potential Depression in a Dense Plasma”. In: Physical Review Letters 109.6 (Aug. 2012).
[18] Thomas Gawne, Thomas Campbell, Alessandro Forte, Patrick Hollebon, et al. “Investigating Mechanisms of State Localization in Highly-Ionized Dense Plasmas”. 2023.
[19] S. X. Hu. “Continuum Lowering and Fermi-Surface Rising in Strongly Coupled and Degenerate Plasmas”. In: Physical Review Letters 119.6 (Aug. 2017).
[20] Yuri Ralchenko, ed. “Modern Methods in Collisional-Radiative Modeling of Plasmas”. Springer International Publishing, 2016.
[21] A. Bar-Shalom, J. Oreg, W. H. Goldstein, D. Shvarts, and A. Zigler. “Super-transition-arrays: A model for the spectral analysis of hot, dense plasma”. In: Physical Review A 40.6 (Sept. 1989), pp. 3183–3193.
[22] A. Bar-Shalom, J. Oreg, and M. Klapisch. “Collisional radiative model for heavy atoms in hot non-local-thermodynamical-equilibrium plasmas”. In: Physical Review E 56.1 (July 1997), R70–R73.
[23] M F Gu. “The flexible atomic code”. In: Canadian Journal of Physics 86.5 (May 2008), pp. 675–689.
[24] A. Bar-Shalom, M. Klapisch, and J. Oreg. “HULLAC, an integrated computer package for atomic processes in plasmas”. In: Journal of Quantitative Spectroscopy and Radiative Transfer 71.2-6 (Oct. 2001), pp. 169–188.
[25] O. Ciricosta, S. M. Vinko, H.-K. Chung, C. Jackson, et al. “Detailed model for hot-dense aluminum plasmas generated by an x-ray free electron laser”. In: Physics of Plasmas 23.2 (Feb. 2016), p. 022707.
[26] H.-K. Chung, M.H. Chen, and R.W. Lee. “Extension of atomic configuration sets of the Non-LTE model in the application to the K diagnostics of hot dense matter”. In: High Energy Density Physics 3.1-2 (May 2007), pp. 57–64.
[27] Q. Y. van den Berg, E. V. Fernandez-Tello, T. Burian, J. Chalupský, et al. “Clocking Femtosecond Collisional Dynamics via Resonant X-Ray Spectroscopy”. In: Physical Review Letters 120.5 (Feb. 2018).
[28] Alberto G. de la Varga, Pedro Velarde, François de Gaufridy, David Portillo, et al. “Non-Maxwellian electron distributions in time-dependent simulations of low-Z materials illuminated by a high-intensity X-ray laser”. In: High Energy Density Physics 9.3 (Sept. 2013), pp. 542–547.
[29] Shenyuan Ren, Yuanfeng Shi, Quincy Y. van den Berg, Muhammad Firmansyah, et al. “Non-thermal evolution of dense plasmas driven by intense x-ray fields”. 2022.
[30] Gareth O. Williams, H.-K. Chung, S. Künzel, V. Hilbert, et al. “Impact of free electron degeneracy on collisional rates in plasmas”. In: Physical Review Research 1.3 (Dec. 2019).
[31] G. O. Williams and M. Fajardo. “Collisional ionization and recombination in degenerate plasmas beyond the free-electron-gas approximation”. In: Physical Review E 102.6 (Dec. 2020).

Implementing the Bethe-Heitler cross section with Neural Networks

Óscar Amaro, Chiara Badiali, Marija Vranic , Bertrand Martinez [1]

***Abstract*— Plasmas in extreme conditions are prone to extensive particle production. These processes need to be properly accounted for in computer simulations; however, standard methods often trade accuracy for speed. In this work we train a neural network to predict the probability distributions of the Bethe-Heitler process required in this computational step, leading to competitive speed, accuracy, and generalization to higher dimensional problems.**

I. INTRODUCTION

Plasmas in extreme conditions of energy and electromagnetic field intensities exhibit highly nonlinear dynamics which need to be properly captured in computer simulations. One of the most common approaches for accurate and self-consistent simulation of such plasma systems is the particle-in-cell (PIC) approach, one example of such a code being the fully-relativistic, massively parallel code `OSIRIS` [1]. The PIC framework has boosted development in applied research fields such as inertial confinement fusion [2], plasma-based particle accelerators [3], laboratory astrophysics [4], quantum electrodynamics, nuclear and particle physics [5].

Despite all this progress, the PIC approach is too computationally expensive to spatially resolve binary processes such as collisions between charged particles. To circumvent this problem, additional modules are necessary, namely Monte-Carlo (MC) routines. These algorithms pair particles together when they are close in phase-space, and evaluate the energy exchange, particle production, or annihilation by sampling the probability density distribution of the process. MC modules have been actively developed for several decades and are now a standard numerical tool [6]–[10].

Numerical modeling of recent and near-future experiments in setups where high intense laser pulses interact with solid targets requires high-fidelity simulation codes (see figure 1a)). These need to resolve not only the classical plasma dynamics (particle trajectories, current and field couplings, etc), but also the quantum/stochastic phenomena that shape the phase-space of the system in very short time-space scales and with creation/depletion of particles. Amongst these phenomena are the lowest-order Coulomb QED processes like Bethe-Heitler and Bremsstrahlung. The former relates to the decay of a gamma-ray photon with energy k in the vicinity of the atomic Coulomb field of an atom with charge Z to produce a positron with energy γ_+ and an electron with energy $k-\gamma_+$, while the later relates to the emission of high energy photons by leptons (see figure 1b)).

[1]GoLP/Instituto de Plasmas e Fusão Nuclear, Instituto Superior Técnico, Universidade de Lisboa, 1049-001 Lisbon, Portugal
Corresponding author: `oscar.amaro@tecnico.ulisboa.pt`

Stochastic production of particles in these extreme environments follows specific probability distributions, which are functions not only of the initial and final (energy) states of the intervening particles, but also of the environment they are in (e.g., the intensity of the electromagnetic field). These probability distributions are used in MC algorithms that are often structured in two steps: first, the "total" cross section (TCS) of the event is computed to determine if a particle is created; second, if this is the case, then the state of the final particle is sampled from the "differential" cross section (CDF). These cross-sections often involve integrals of special mathematical functions or other expensive subroutines, which rendered their computation in run-time inefficient in early-day MC codes.

Some solutions have been proposed for the calculation of these processes; however, there is often a trade-off between speed, accuracy, and generality. For example, some codes include look-up tables for interpolation in runtime, which although fast, can lead to significant memory usage (which grows exponentially with the number of dimensions of the input parameters), clutter the code and lead to nonphysical numerical artifacts.

Several particle-in-cell codes have been added modules to simulate the Bethe-Heitler process [11]–[13]. In particular, in [13] this implementation, although accurate, depends on look-up tables, which can take up significant memory in the code, and usually only applies to a limited set of Z materials.

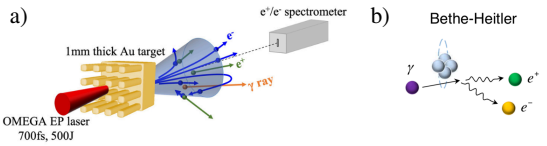

Fig. 1. a) Schematic of setup where intense laser interacts with a gold target, producing pairs [14]. b) Schematic of the Bethe-Heitler processe [13].

Besides look-up tables, there are relatively few alternatives explored in the literature. In [15] the authors implement Chebyshev polynomial approximations of the rates, which is more efficient and accurate than the standard table interpolation. However, the number of Chebyshev coefficients for 3D or higher input space functions is impractical, meaning the method does not generalize well for high dimensional problems.

In contrast, Dense Artificial Neural Networks (NN) are routinely used as efficient, accurate and compact models for data regression [16], [17].

In this work we prepare the stage to replace part of

the MC routine of the OSIRIS code for the Bethe-Heitler process with two neural networks. The resulting well-trained and optimized NNs enable fast and accurate evaluation, reduced memory storage and ability to generalize well to problems where probability rates depend on many input parameters (high-dimensionality), thereby solving the three issues identified in the literature. This was already proven in the context of Inertial Confinement Fusion (ICF) where NNs demonstrated to speed up the run-time evaluation of spectral opacities in non-local thermal equilibrium in the hydro-rad code HYDRA to model an ICF hohlraum [18]. Our numerical framework builds upon the work developed by Badiali et al [19] and adapt it to implement the Bethe-Heitler cross section.

This report is structured as follows: in section II we explain how the datasets for the Bethe-Heitler cross sections were produced; in section III we detail the machine learning approach used in this work; in IV we present the main results of this work; finally, in V we present the main conclusions and list possible future steps in this project.

II. Data generation and preparation

In this section we explain how datasets for the training of the model were generated, "prepared" and "balanced".

Generating the data: contrary to the case of [19], our training data does not originate from `OSIRIS` simulations. Instead, simple scripts compute the analytical cross sections and their transformations such as the CDF and the TCS. Initially, the scripts to generate the data were written in `Python` and were used to produce datasets of circa 1 million entries for the two cross-sections, where the first columns represented the input parameters and the last column the target value. To attempt a more representative dataset over the input domain, variables were generated from the grids: $Z \in [1, 100]$ (linspace), $k \in [2.1, 2 \times 10^4]\ m_e c^2$ (logspace) and $\gamma_+/k \in [0, 1]$ (linspace), where linspace represents a uniformly spaced sequence of number over the respective interval (and logspace the equivalent uniformly spaced sequence over the logarithm of the interval).

Preparing the data: over this input domain the TCS can range between 10^{-32} and 10^{-26} m^2 . Instead, we normalize the data to become close to the interval $[0, 1]$. One such transformation is taking the negative logarithm of the cross-section and then to normalize this quantity. In contrast, the CDF is by definition already in the range $[0, 1]$. However, for all parameters this curve is always close to CDF $\sim \gamma_+/k$, which makes it difficult for the model to distinguish between different input combinations. Instead, we create a new variable CDF $- \gamma_+/k$, such that the model learns this difference. We proceed to normalize this variable to the range $[0, 1]$.

Balancing the data: since the cross sections are very nonlinear functions of the input parameters, some values of the target can occur many orders of magnitude more often than other. This leads the NN to disregard the statistically rare entries and to perform poorly on the entire input domain. Several approaches exist to avoid this issue. In this work we apply an algorithm that takes a dataset and reduces the frequency of the over-represented entries and oversamples the under-represented until achieving a value close to the average, producing a new dataset with approximately the same number of entries as the original one.

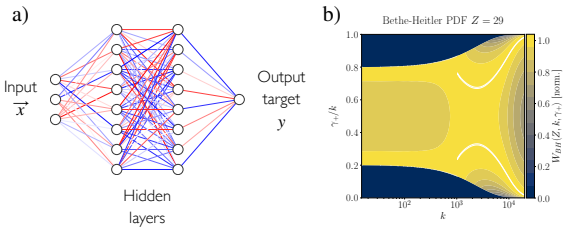

Fig. 2. a) Schematic of a representative Neural Network architecture used in this work. b) Contourplot of the Bethe-Heitler differential cross-section, showcasing the symmetry around $\gamma_+ = k/2$.

Whereas the main goal of data preparation is to change the interval of the target values, the goal of data balancing is to then change the distribution of the prepared data over this new interval.

After testing the initial input domain of parameters, we observed that the model was having some trouble learning the cases when the CDF was close to 0 (which happens when $\gamma_+/k \to 0$). We then decided to halve the domain (using the symmetry of the cross section) such that $\gamma_+/k \in [0.5, 1]$. This choice appeared to resolve the previous issue. Since the input domain was now smaller, a second random number (1 bit) would then be needed to decide if the produced particle has energy γ_+ (positron) or $k - \gamma_+$ (electron).

After training of the model, the output of the neural network needs to be translated back to real units, reversing the data preparation step.

III. Model Training

In this section we describe the machine learning approach followed in this project.

We train fully connected-layers, dense Deep Neural Networks (DNNs) with varying number of inputs, hidden layers (< 4 hidden layers), but always with 1D output, since the goal is to learn scalar probability distribution functions (see figure 2). We choose this approach over alternative architectures such as Convolutional or Recurrent Neural Networks because of their simplicity and compactness.

We use the `Keras` framework [20] to build and train the neural network, the `Python` libraries `Numpy`, `Pandas` and `Scipy`, and `C++` using the boost scientific library [21]. Training is carried out until the loss (a measure of the distance between the prediction of the network and the real values) has decreased significantly and stabilized. In this work we assume that the plasma temperature is $T = 0$ keV (cold) and particles are unpolarized, which is usually a good first approximation, that could nevertheless be made more complex in the future. By definition the CDF is monotonic; however this behavior is not explicitly enforced in the NN.

If the accuracy of the model is sufficiently high, this issue can be mitigated.

Contrary to [19], in this work we are not replacing the MC routine with a conceptually different approach; instead, we are replacing the computation of the TCS and the CDF within the MC module by a possibly more efficient and scalable approach.

For both cross sections, the activation function between layers is `ReLU`, the output node has a Sigmoid activation function and the optimizer used was `Adam`. In the case of the TCS, the loss function and the metric were `mape` and `binary cross entropy`, respectively, while for the CDF these were `mae` and `mape`. Several approaches were found to improve the training of the NNs, namely data balancing, batch normalisation and increasing the number of entries of the dataset (see section II).

Additionally, it was observed that the CDF NN could not accurately reproduce the data when γ_+ and the CDF were close to 0. Since the CDF presents some symmetry around $\gamma_+ = k/2$, the information contained in the intervals $\gamma_+/k \in [0, 0.5]$ and $\gamma_+/k \in [0.5, 1]$ is the same. Therefore, we split the datasets into these two cases, and verified that the trained models performed better in the interval $[0.5, 1]$.

IV. Results

In this section we report the results of the training of the networks.

For the TCS, the layout with two layers, 12-12 nodes presented the best results, having obtained an average relative error on the order of 5 % (see figure 3).

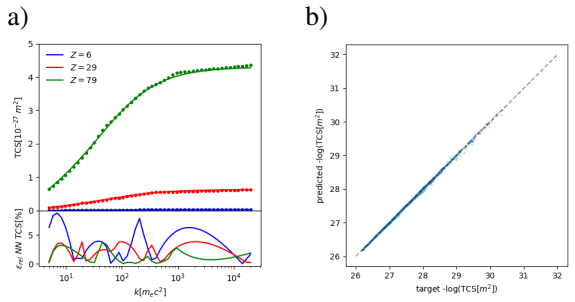

Fig. 3. Results for the total cross section: a) Evaluating the NN model prediction against theoretical results for specific parameters, b) Evaluating the NN model prediction against theoretical results for all training data.

In the case of the CDF, the best performing architecture was the 3 layers, 8-16-8 nodes, for which we obtained an average relative error below 0.1% (see figure 4).

These results report to a later stage of the project, when it was decided that larger datasets were required, going from 1 million to 10 million entries both for the TCS and CDF. The choices of nodes per layer referred previously for the NNs led the TCS have 209 trainable parameters, while the CDF has 327. This contrasts with the look-up table approach described in section I, which can require around 800 parameters per atomic number.

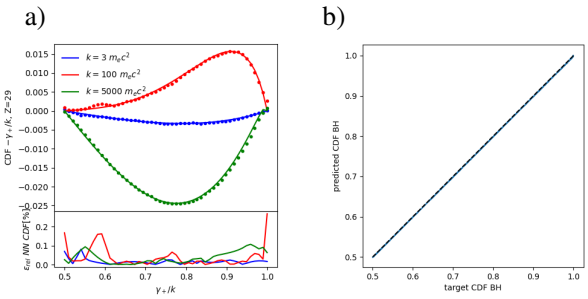

Fig. 4. Results for the differential cross section: a) Evaluating the NN model prediction against theoretical results for specific parameters, b) Evaluating the NN model prediction against theoretical results for all training data.

V. Conclusions

In this work we have presented initial results from the training of neural networks to approximate probability distributions used in Monte-Carlo simulations in plasma physics. Two distributions were considered: the total cross section of the Bethe-Heitler pair production process and the associated cumulative distribution function of the differential cross section. In the former, we obtained an average relative error on the order of 5 %, whereas for the later we obtained below 0.1%. From the models tested, the choice of 2 hidden layers with number of nodes $12 - 12$ for the TCS and 3 hidden layers with number of nodes $8 - 16 - 8$ for the CDF gave the best accuracy. These trained models are now very close to being implemented in a production code.

As future work, we will implement the trained neural networks in OSIRIS and compare the performance/accuracy to the look-up table.

Despite having focused on the Bethe-Heitler process in this work, our approach can be generalised to any process relevant in plasma physics (Coulomb deflections, impact ionisation, three-body recombination, D-T fusion), in atomic physics (atomic de-excitation) and radiative transport (photo-ionisation, radiative recombination, Compton scattering).

References

[1] R. A. Fonseca, L. O. Silva, F. S. Tsung, V. K. Decyk, W. Lu, C. Ren, W. B. Mori, S. Deng, S. Lee, T. Katsouleas, and J. C. Adam, "OSIRIS: A Three-Dimensional, Fully Relativistic Particle in Cell Code for Modeling Plasma Based Accelerators," in *Computational Science — ICCS 2002*, ser. Lecture Notes in Computer Science, P. M. A. Sloot, A. G. Hoekstra, C. J. K. Tan, and J. J. Dongarra, Eds. Berlin, Heidelberg: Springer, 2002, pp. 342–351.

[2] J. Lindl, "Development of the indirect-drive approach to inertial confinement fusion and the target physics basis for ignition and gain," *Physics of Plasmas*, vol. 2, no. 11, pp. 3933–4024, Nov. 1995.

[3] E. Esarey, P. Sprangle, J. Krall, and A. Ting, "Overview of plasma-based accelerator concepts," *IEEE Transactions on Plasma Science*, vol. 24, no. 2, pp. 252–288, Apr. 1996.

[4] R. D. Blandford and C. F. McKee, "Radiation from relativistic blast waves in quasars and active galactic nuclei," *Monthly Notices of the Royal Astronomical Society*, vol. 180, no. 3, pp. 343–371, Oct. 1977.

[5] A. Di Piazza, C. Müller, K. Z. Hatsagortsyan, and C. H. Keitel, "Extremely high-intensity laser interactions with fundamental quantum systems," *Reviews of Modern Physics*, vol. 84, no. 3, pp. 1177–1228, Aug. 2012.

[6] T. Takizuka and H. Abe, "A binary collision model for plasma simulation with a particle code," *Journal of Computational Physics*, vol. 25, no. 3, pp. 205–219, Nov. 1977.

[7] K. Nanbu, "Theory of cumulative small-angle collisions in plasmas," *Physical Review E*, vol. 55, no. 4, pp. 4642–4652, Apr. 1997.

[8] Y. Sentoku and A. J. Kemp, "Numerical methods for particle simulations at extreme densities and temperatures: Weighted particles, relativistic collisions and reduced currents," *Journal of Computational Physics*, vol. 227, no. 14, pp. 6846–6861, Jul. 2008.

[9] F. Peano, M. Marti, L. O. Silva, and G. Coppa, "Statistical kinetic treatment of relativistic binary collisions," *Physical Review E*, vol. 79, no. 2, p. 025701, Feb. 2009.

[10] F. Pérez, L. Gremillet, A. Decoster, M. Drouin, and E. Lefebvre, "Improved modeling of relativistic collisions and collisional ionization in particle-in-cell codes," *Physics of Plasmas*, vol. 19, no. 8, p. 083104, Aug. 2012.

[11] T. Moritaka, L. Baiotti, A. Lin, L. Weiwu, Y. Sakawa, Y. Kuramitsu, T. Morita, and H. Takabe, "Plasma particle-in-cell simulations with QED reactions for pair production experiments using a high-Z solid target," *Journal of Physics: Conference Series*, vol. 454, no. 1, p. 012016, Aug. 2013.

[12] T. Nakamura and T. Hayakawa, "Numerical modeling of quantum beam generation from ultra-intense laser-matter interactions," *Laser and Particle Beams*, vol. 33, no. 2, pp. 151–155, Jun. 2015.

[13] B. Martinez, M. Lobet, R. Duclous, E. d'Humières, and L. Gremillet, "High-energy radiation and pair production by Coulomb processes in particle-in-cell simulations," *Physics of Plasmas*, vol. 26, no. 10, p. 103109, Oct. 2019.

[14] S. Jiang, A. Link, D. Canning, J. A. Fooks, P. A. Kempler, S. Kerr, J. Kim, M. Krieger, N. S. Lewis, R. Wallace, G. J. Williams, S. Yalamanchili, and H. Chen, "Enhancing positron production using front surface target structures," *Applied Physics Letters*, vol. 118, no. 9, p. 094101, Mar. 2021.

[15] S. Montefiori and M. Tamburini, "SFQEDtoolkit: A high-performance library for the accurate modeling of strong-field QED processes in PIC and Monte Carlo codes," Jan. 2023.

[16] F. Chollet, *Deep Learning with Python*, 1st ed. Shelter Island, New York: Manning Publications Co, 2018.

[17] A. Géron, *Hands-On Machine Learning with Scikit-Learn, Keras, and TensorFlow: Concepts, Tools, and Techniques to Build Intelligent Systems*. "O'Reilly Media, Inc.", Sep. 2019.

[18] G. Kluth, K. D. Humbird, B. K. Spears, J. L. Peterson, H. A. Scott, M. V. Patel, J. Koning, M. Marinak, L. Divol, and C. V. Young, "Deep learning for NLTE spectral opacities," *Physics of Plasmas*, vol. 27, no. 5, p. 052707, May 2020.

[19] C. Badiali, P. J. Bilbao, F. Cruz, and L. O. Silva, "Machine-learning-based models in particle-in-cell codes for advanced physics extensions," *Journal of Plasma Physics*, vol. 88, no. 6, p. 895880602, Dec. 2022.

[20] F. Chollet *et al.*, "Keras," https://keras.io, 2015.

[21] "Boost C++ Libraries," https://www.boost.org/.

centra

ipfn

INSTITUTO DE PLASMAS
E FUSÃO NUCLEAR

FCT

Fundação para a Ciência e a Tecnologia

MINISTÉRIO DA EDUCAÇÃO E CIÊNCIA

TÉCNICO
LISBOA